Journal of Materials Chemistry C

Photoluminescence Detection of Symmetry Transformations in Low-dimensional Ferroelectric ABO_3 Perovskites

Journal:	*Journal of Materials Chemistry C*
Manuscript ID	TC-ART-03-2020-001183.R1
Article Type:	Paper
Date Submitted by the Author:	08-Apr-2020
Complete List of Authors:	Ofoegbuna, Tochukwu; Louisiana State University, R. Bajgiran, Khashayar; Louisiana State University, Cain Department of Chemical Engineering Kizilkaya, Orhan; Louisiana State University, CAMD Thomson, Stuart; Edinburgh Instruments Ltd Melvin, Adam; Louisiana State University, Cain Department of Chemical Engineering Dorman, James; Louisiana State University, Chemical Engineering

ARTICLE

Photoluminescence Detection of Symmetry Transformations in Low-dimensional Ferroelectric ABO_3 Perovskites

Received 00th January 20xx,
Accepted 00th January 20xx

DOI: 10.1039/x0xx00000x

Tochukwu Ofoegbuna,[a] Khashayar R. Bajgiran,[a] Orhan Kizilkaya,[b] Stuart A. J. Thomson,[c] Adam T. Melvin,[a] and James A. Dorman *[a]

Symmetry-dependent properties such as ferroelectricity are suppressed at room temperature in Pb-free ABO_3 perovskites due to antiferrodistortive dynamics (octahedral rotations/tilts), resulting in the preferential stabilization of centrosymmetric crystals. For this reason, defect engineering (Ca doping, Oxygen vacancy, etc.) has been leveraged to break the symmetry of these crystals by inducing symmetry/structural transitions to modify the local A/B-site environment. This work demonstrates the use of *in-situ/ex-situ* photoluminescence spectroscopy to systematically detect symmetry/structural transformations in prototypical ferroelectric ABO_3 perovskites. These baseline optical responses are compared to recently synthesized $Ca_xSr_{1-x}NbO_3$ (CSNO) nanocrystals, which undergoes similar ferroelectric/structural phase transitions. Furthermore, the resultant PL response is corroborated with X-ray diffraction (XRD) and absorption spectroscopy (XAS) measurements to confirm the structural changes. This ability to directly monitor the local site symmetry within ABO_3 perovskites via photoluminescence spectroscopy can be used to screen for temperature- and defect-induced ferroelectric transitions.

1. Introduction

The future of renewable energy sources relies on the discovery of new materials for high density energy storage.[1] Owing to their multi-functionality, high polarization potential, and dielectric constant, ferroelectric (FE) ABO_3 (A, B = various metal ions) perovskites are a popular class of materials for capacitor technology.[2, 3] $PbTiO_3$ and similar perovskite based capacitors exhibit exceptional energy storage density due to the off-center hybridization of the A-site (Pb) with O.[3] However, the toxic nature of Pb limits their commercial use necessitating Pb-free FE replacements.[4] Unfortunately, FE instabilities are suppressed in Pb-free ABO_3 perovskites at room temperature due to antiferrodistortive (AFD) distortions of the BO_6 octahedral rotations/tilts, resulting in the preferential stabilization of the centrosymmetric *Pnma* space group.[5] Defect engineering (Ca doping, Oxygen vacancy, etc.) has been effectively utilized to overcome these AFD distortions by modifying the local A/B-site symmetry in ABO_3 perovskites.[6] Traditionally, the effect of these defects on the overall FE response has been monitored using scanning probe microscopy techniques such as Piezoresponse Force Microscopy (PFM).[7] However, studying the defect-induced FE response is a challenge for traditional PFM-based characterization due to the application of large electric fields, which inadvertently results in significant changes to the local structure.[8, 9] Thus, PFM-based methods are prone to erroneously interpret electrostatic forces, non-piezoelectric electromechanical, and surface/bulk electrochemical phenomena as FE polarization.[7, 9] One approach which has yet to be fully investigated is the use of structurally-dependent photoluminescent probes, such as Eu^{3+}.[10, 11] This method has been applied to study the local crystal and electronic structure of *p*-type GaN.[12-15] Furthermore, the use of Eu^{3+} as a probe has resulted in new information regarding structural transformations in Ruddlesden–Popper (RP)-type materials,[16] and can potentially be extended to the screening of FE ABO_3 perovskites.[17] In particular, the effect of defects on the A/B-site symmetry can be systematically studied by comparing the symmetry-dependent optical transitions ($^5D_0$-$^7F_1$ and $^5D_0$-$^7F_2$).[17-19] Therefore, this work aims to utilize structural defects to destabilize the centrosymmetry of Pb-free ABO_3 perovskites and probe the resultant structural changes using Eu^{3+} photoluminescence.[5, 9, 20]

Among the prototypical perovskite oxides, strontium titanate ($SrTiO_3$, STO) is known as a model system for studying defect-induced properties which arise from symmetry transformations.[20, 21] For instance, upon Ca doping STO, local dipoles are induced by the off-center Ca ions which breaks the centrosymmetry of the A-site and results in a macroscopic FE

[a] *Cain Department of Chemical Engineering, Louisiana State University, Baton Rouge, Louisiana 70803, United States. Email: jamesdorman@lsu.edu.*
[b] *Center for Advanced Microstructure Devices, Louisiana State University, Baton Rouge, Louisiana 70803, United States.*
[c] *Edinburgh Instruments Ltd., 2 Bain Square, Livingston EH54 7DQ, United Kingdom.*

†Electronic Supplementary Information (ESI) available: XRD pattern and Raman spectra for $Ca_xSr_{1-x}TiO_3$:Eu (2 mol%) NPs, Rietveld refinement of $Ca_xSr_{1-x}NbO_3$: Eu (2 mol%, x = 0 and 1.0) NPs, refined atomic coordinates and structural parameters from GSAS II, schematic representation of structure transformation from Ca-doping, PL emission spectra and lifetime for $Ca_xSr_{1-x}NbO_3$: Eu (2 mol%) NPs, and XRD pattern for $(Ba,Pb)TiO_3$ NPs. See DOI: 10.1039/x0xx00000x

response.[22] Along this line, strontium niobate ($SrNbO_3$, SNO) has become the subject of experimental[23] and theoretical[24] studies due to its interesting plasmonic and photocatalytic applications. Furthermore, coupling its previously reported[25] low-loss response with FE behavior will make it a promising candidate material for multiple FE applications.[26, 27] Unfortunately, traditional wet-chemical approaches[28-30] result in the thermodynamically stable pentavalent state of Nb,[31] necessitating the need for low-pressure deposition methods. To limit the preferential seeding of this oxidation state via solution-based chemistries, oxygen-deficient atmospheres were leveraged to successfully synthesize SNO NPs (~ 20 nm).[32] The formation of SNO was further favored using a critical Sr/Nb concentration of 1.3. In the present work, $Ca_xSr_{1-x}NbO_3$: Eu (2 mol%, CSNO) NPs were synthesized using this technique. In order to study the effect of Ca incorporation on the formation of structural/FE phase transitions in CSNO, *in-situ*(applied temperatures)*/ex-situ*(crystal composition) photoluminescence (PL) spectroscopy was performed and compared against CSTO, BTO, and PTO NPs. This *in-situ/ex-situ* PL study was compared to standard X-ray diffraction (XRD) and absorption spectroscopy (XAS) techniques to quantify the local and extended crystal structures.

2. Experimental

2.1 Synthesis of $Ca_xSr_{1-x}NbO_3$: Eu (2 mol%, CSNO) Nanocrystals

CSNO (x = 0, 0.1, 0.2, 0.5, 0.8, and 1.0) nanoparticles were synthesized using a two-step co-precipitation/ oxygen-controlled crystallization approach described in detail elsewhere.[32] Briefly, A-site ($Sr(NO_3)_2$, Alfa Aesar, 99.0%, ACS grade; $Ca(NO_3)_2$-H_2O, Beantown Chemical, 99.9995% trace metals basis; $Eu(NO_3)_2$-$6H_2O$, Alfa Aesar, 99.99% REO) and B-site ($NbCl_5$, Alfa Aesar, 99.0% metals basis) salt precursors were precipitated using ammonium hydroxide (NH_4OH, 28-30%, ACS grade) at a pH of 9.5. Next, the as-prepared powder was ground with a eutectic molar ratio of $NaNO_3$ (high purity grade, VWR Amresco, 99.0%) and KNO_3 (VWR Amresco, ACS grade) to form a homogeneous powder. The mixture was then transferred to a porcelain boat and heated in a tube furnace at 600 °C under H_2/Ar atmosphere for 2 h. After cooling, the resultant powder was washed several times with deionized water and dried overnight at 100 °C.

2.2 Characterization

The crystal structure of the NPs was identified by performing Powder X-ray Diffraction (XRD) using PANalytical X-ray diffractometer operating at 45 kV and 40 mA. The θ-2θ radial scan was performed over the range 5-70º with a step size of 0.04º and dwell time of 60 s, using Cu K_α (λ=1.54 Å) as the radiation source. Rietveld refinement was performed on the (Sr, Ca)NbO_3 diffraction pattern using the GSAS II software[33] for structural verification. Full structural refinement was achieved by performing the procedure outlined in ref 23.

Raman spectroscopy was performed via a Renishaw inVia Reflex Raman Spectrometer with a 0.05 mW diode laser at an excitation wavelength of 532 nm, exposure time of 0.5 s, and spectral resolution of 1 cm^{-1}. The diameter of the focused laser spot on the sample at 50x magnification was approximately 5 µm. Three scans were averaged to obtain the reported spectra. For peak deconvolution, the background was subtracted from the resulting spectra to resolve the active modes.

X-ray absorption spectroscopy (XAS) was performed to probe local electronic structural changes to corroborate observed bulk structural transformation from dopant incorporation. XAS measurements were conducted at the varied-line-spaced plane grating monochromator (VLSPGM, 0.2-1.2 keV) beamline of the Center for Advanced Microstructures and Devices (CAMD). In these measurements, changes in the local geometry and electronic structure of the crystal were studied by probing the X-ray absorption near edge spectroscopy (XANES) region of Ca ($L_{3,2}$-edge, ~348 eV) and O (K-edge, ~530 eV). The powder samples were attached to carbon tape and loaded into the sample chamber maintained at 2×10^{-9} Torr. The XANES data, collected with total electron yield mode, was normalized and analyzed with the Athena software.[34] Calcium oxide (CaO, Aldrich, 99.9% trace metals basis) powder was used as a reference for calibration purposes.

To correlate structural modifications to local changes in the A-site symmetry, *in-situ*/*ex-situ* PL spectroscopy was performed. *In-situ* refers to FE/structural changes that are actively being monitored under the application of an external stimuli (i.e. temperature) and *ex-situ* refers to FE/structural changes investigated using samples containing various Ca concentrations. The *ex-situ* PL spectra were measured using an Edinburgh Instruments FLS1000 PL spectrometer equipped with a PMT detector and a 450 W ozone-free xenon arc lamp as the light source. Excitation and emission scans were collected with a 4 nm bandpass at a scan rate of 0.4 nm/s in the range of 240-400 nm (excitation) and 550-650 nm (emission) with 1 nm step size. The powder samples were dispersed onto a quartz sample holder for PL measurements. The lifetime measurements were performed with a microsecond flash lamp (frequency: 25 Hz) over the range of 10 ms. For the *in-situ* temperature-dependent PL measurements, a LINKAM THMS600 temperature-controlled stage was added to the spectrometer setup. Liquid nitrogen was used as the cooling agent. Measurements were performed from -180 to 100 ^oC in 20 ^oC steps. The reported spectra are an average of three scans.

3. Results and discussion

$Ca_xSr_{1-x}NbO_3$ (CSNO) nanocrystals were synthesized as a promising Pb-free FE alternative using an oxygen-deficient wet-chemical method (refer to the Experimental Section in ESI† for details). This synthetic method limits available oxygen during the crystallization process allowing for systematic control of defects. Previously, it was reported that FE instabilities in bulk/thin-film can be stabilized by controlling defect formation,[8, 9] therefore, an analogous approach was implemented using Ca doping during the NP growth. The XRD patterns of the CSNO NPs affirm the crystallization of cubic (C, $SrNbO_3$) and orthorhombic (O, $CaNbO_3$) phases (Fig. 1). Four

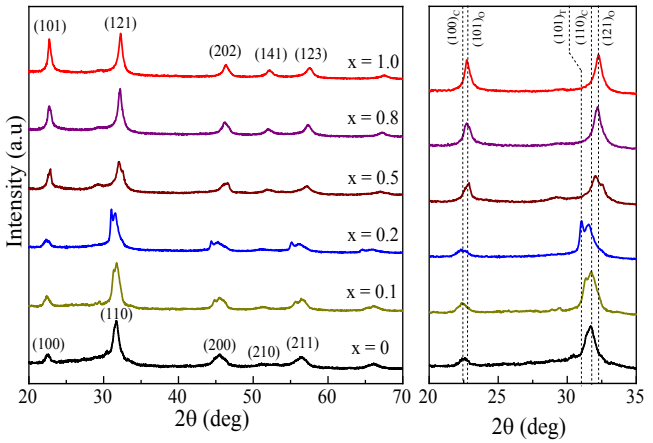

Fig. 1 Diffraction pattern for CSNO:Eu (2 mol%) nanoparticles. Enlarged view of the diffraction pattern (in the range of 2θ = 20-40) to highlight the formation of T and O reflections. Miller indices are based on $Sr_{0.7}NbO_3$ (ICDD 19-2410) and $CaNbO_3$ (ICDD 47-1668) references.

intermediate doping concentrations (x = 0.1, 0.2, 0.5, and 0.8) are also shown along with a magnified view in the 2θ range of 20 to 35°. Additionally, Rietveld refinement (Fig. S1 and Table S1, ESI†) was performed using $Sr_{0.7}NbO_3$ (*Pm-3m*, ICDD 19-2410) and $CaNbO_3$ (*Pnma*, ICDD 47-1668) as structural references for the C and O phases, respectively. Good statistical (R_p, R_{wp} < 10% and χ^2 < 5) and visual agreements were observed for these models. The compounds with low Ca concentration (x = 0.1 and 0.2) exhibit what appears to be a shift toward the tetragonal (T) phase based on a comparison with STO (ICDD 70-6460). However, the fitting of these structures was not able to be performed since no structural models are available. The change from C to T phase with Ca composition can be seen from the presence of $(100)_C$, $(110)_C$, and $(101)_T$ peaks. At x = 0.5, the crystal is a mixture of phases, based on the constant peak splitting as well as the shift in the diffraction peak to higher angles. A pure O phase is formed when x > 0.8, as evident from the appearance of $(101)_O$ and $(121)_O$ reflections. The calculated lattice parameters and cell volumes are listed in Table S2 (ESI†).

XAS analysis was performed to confirm these symmetry/structural transformations. This technique is sensitive to changes in the local (<10 Å) geometric and electronic structure around the X-ray absorbing atom.[35, 36] Figs. 2a and 2b show the normalized Ca $L_{3,2}$-edge and O K-edge XANES spectra of the CSNO NPs along with a CaO reference spectrum. The Ca L-edge spectra are divided into the L_3-edge (electron transition from $2p_{3/2}$ to 3*d*, ~349 eV) and the L_2-edge (electron transition from $2p_{1/2}$ to 3*d*, ~353 eV), appearing due to large 2*p* core hole spin-orbit coupling.[37] The major features observed in the Ca $L_{3,2}$-edge XANES spectra, denoted as **a_1**, **a_2**, **b_1**, and **b_2**, are predominantly attributed to the spin-orbit coupling of Ca 2*p* core states and the splitting of the 3*d* orbitals due to the crystal-field by surrounding O ions.[38, 39] For all investigated CSNO samples, the Ca $L_{3,2}$-edge XANES spectra (data for x = 0 is not shown since there is no Ca atom) shows

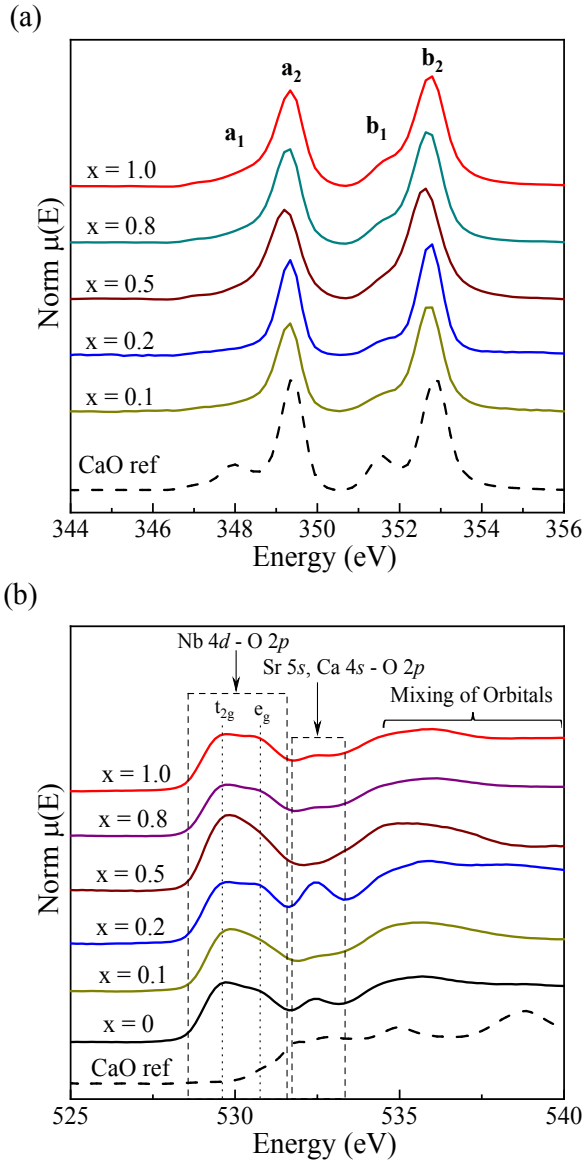

Fig. 2 (a) Ca L-edge and (b) O K-edge XANES spectra of CSNO:Eu (2 mol%) nanoparticles. The CaO reference spectra are displayed as dashed lines.

significant reduction to the **a_1** and **b_1** peak intensities. This peak reduction confirms that Ca doped into the CSNO lattice is incorporated into the A-site (CaO_{12}) rather than the B-site (CaO_6), as a spectrum similar to the CaO reference would be expected for octahedrally coordinated Ca.[40] The O K-edge XANES spectra were collected to verify that the presence of Ca in the A-site is responsible for the structural changes observed in the CSNO NPs. The three spectral features observed in the O K-edge spectra are ascribed to the hybridization of Nb 4*d*-O 2*p* (~528.5-531.5 eV), the hybridization of Sr 5*s*/Ca 4*s*-O 2*p* (~532.4 eV), and the additional visible small peaks (~533.3-540.0 eV) are attributed to the mixing of Nb 5*sp*/Ca 4*sp*-O 2*p* orbitals.[41, 42] From the XANES spectra, Ca doping to the onset of phase transition (x = 0.1 and 0.5), results in a loss of definition in the hybridized Nb 4*d* (e_g orbital) and Sr 5*s*/Ca 4*s* peaks. Similar spectral changes have been observed for $Ba_xLa_{1-x}MnO_3$ which

undergoes a C (x = 0) to H (hexagonal, x = 1) phase transition.[43] This suggests that there is no long-range ordering as these phase transitions occur and therefore, a disordered cubic structure accurately describe these systems.[35, 44]

Model CSTO:Eu, BTO:Eu, and PTO:Eu (2 mol%) NPs were synthesized as references for the composition and temperature-induced phase transitions.[45-48] XRD of the CSTO (Fig. S3a, ESI†) affirms the crystallization of C (*Pm-3m*), T (*I4/mcm*), and O (*Pnma*) phases at the same Ca concentrations as in CSNO and agrees with literature values for these expected phases.[49] The assigned phases are further validated using Raman spectroscopy (Fig. S3b, ESI†), which highlights the formation of new vibrational modes with increased Ca incorporation. These modes are labeled according to literature.[50-52] The XRD patterns (Fig. S4a and S4b, ESI†) confirm the formation of BTO (*P4mm*, ICDD 5-0626) and PTO (*P4mm*, ICDD 6-0452) in T phase.

The symmetry changes in the A-site environment induced from the reconstruction of the CSTO and CSNO lattice as a result of Ca doping was probed using *ex-situ* PL spectroscopy. The collected emission spectra and extracted asymmetry ratio (emission intensity ratio of $^5D_0$-$^7F_1$ and $^5D_0$-$^7F_2$, R-value)[17, 18] for the C (x = 0), T(x = 0.2), and O (x = 0.8) phases, are shown in Figs. 3 and S2 (ESI†). The horizontal dashed lines indicate the measured R-values for STO, BTO, and PTO NPs. As shown in Fig. 3, for the CSTO NPs, an increase in the R-value (reduction in

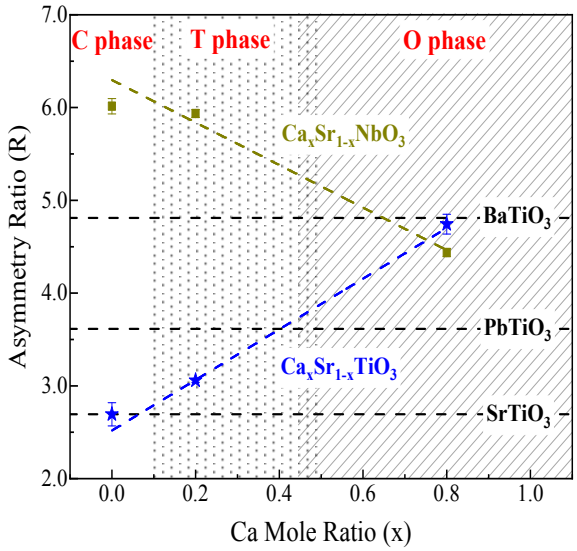

Fig. 3 Asymmetry ratio (R) for CSNO:Eu, CSTO:Eu, BTO:Eu, and PTO:Eu (2 mol%) nanoparticles. The dashed lines are a guide for the eye. C, T, and O phase identifications are based on XRD and XAS results.

symmetry) is observed and this is consistent with the XRD trend, i.e., C to T and T to O (from 2.7 ± 0.1 to 4.7 ± 0.1). This increasing trend signifies that the crystallographic symmetry (long-range structure) mirrors the spectroscopic symmetry (local structure).[17] Although similar responses have been reported in literature for CSTO (where x is 0 and 1.0),[53, 54] these results demonstrate that, in addition to starting and final phases, intermediate phases can also be identified using PL.

Interestingly, the observed R-value for CSNO (6.0 ± 0.1) does not significantly change when x < 0.2, suggesting that initial structural changes occur gradually possibly due to the presence of two phases. These observations also coincide with the XRD results. At higher doping concentrations, the R-value decreases (4.4 ± 0.1) suggesting a higher symmetry site surrounding the Eu^{3+} ion, counter to what is seen for CSTO. The difference in the PL response with Ca doping is attributed to the CSTO being synthesized using a reported hydrothermal route where less oxygen defects are present. However, this approach is not suitable for stabilizing the Nb oxidation state, motivating the need for the low-pressure synthetic method. It is believed that the presence of defects (Oxygen vacancy) surrounding the A-site is responsible for this high R-value which subsequently decreases with increasing Ca concentration. PL lifetime experiments (Fig. S5 and Table S2, ESI†) were performed on the CSNO samples to probe the composition-induced symmetry change. As with the other characterization methods, the lifetime measurements of x = 0 and 0.2 did not show significant changes (i.e. within fitting error). At higher Ca concentrations (x = 0.8), a pronounced increase (> 200 µs) is observed in the lifetime and this is attributed to the formation of the O phase.[16]

In-situ PL measurements were performed to probe the effect of Ca incorporation on the crystal structure at temperatures where AFD distortions are suppressed. Due to the highly local nature of the probing method, standard deviation change, slope change, etc. are good indicators of FE/structural transitions.[16] As there is a large body of work pertaining to the FE/structural transition temperatures of BTO, PTO, and CSTO,[55-58] these crystals are well-suited to initially test the *in-situ* method before being applied to the material of interest (CSNO). Initially, Eu^{3+}-doped $NaYF_4$ (*Fm-3m*, Fig. S6, ESI†) NPs in C phase

Table 1 Transition temperatures for select FE perovskite oxides

Chemical Composition	Transition Temperature (Bulk, °C)[a]	Transition Temperature (Local, °C)[b]	Ref.
BTO	-80 and 0	-120 and 30	55
PTO	-100	-100	56
STO	-233[c] and -190[c]	-50	57, 58
CSTO	-233[c] to -150	0	58

[a]Bulk comes from literature.
[b]Local comes from our work using *in-situ* PL measurements.
[c]Temperatures below *in-situ* PL measurement range.

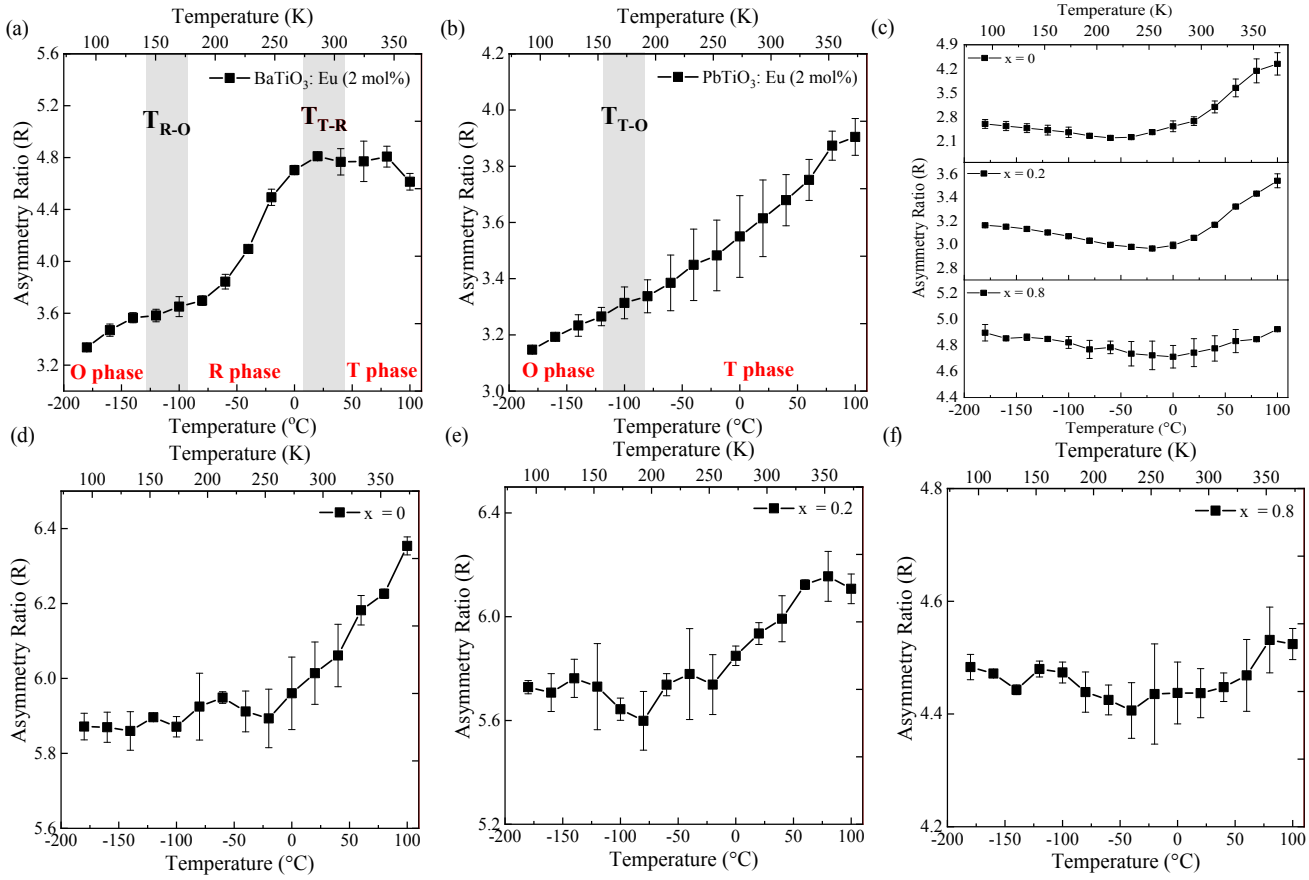

Fig. 4 *In-situ* temperature-dependent PL for (a) BTO:Eu, (b) PTO:Eu, (c) CSTO:Eu and (d-f) CSNO:Eu (2 mol%) nanoparticles. The PL emission spectra were collected with an excitation of 395 nm. The C, T, O, and R phases are indicated in the BTO and PTO plots.

were used as a control[59, 60] to verify that any observed changes to the R-value for the ABO_3 perovskites are due to FE/structural transitions. The reference $NaYF_4$ sample showed little change with temperature (1.91 ± 0.02) indicating that the R-value is independent of temperature without structural changes. The temperature-dependent PL measurement on BTO (Fig. 4a) shows a pronounced drop in the R-value starting at 25 °C and leveling off around -100 °C and this coincides well with reported T to R and R to O structural transition temperatures.[55] In the case of PTO, the low-temperature T to O phase change (-100 °C, Table 1) only slightly distorts the crystal (a/b~1.0002).[56] At this temperature, there is a distinct decrease in signal standard deviation from ±0.1 to ±0.03 which is attributed to long-range ordering in the NP crystal structure (Fig. 4b). Similar temperature-dependent analysis of CSTO (Fig. 4c) shows that the R-value begins to increase when the temperature drops below -50 °C for x = 0 and at around -20 °C for x = 0.2 due to the start of the C to T phase transformation. According to reported XRD/dielectric experiments (Table 1),[57, 58] the C to T transition temperatures are expected to fall outside the PL capabilities and, thus could not be determined. The temperatures listed in Table 1, identified using bulk techniques, provide information regarding the global structure. However, the temperatures, extracted using PL, examine the local structure allowing for both the start (non-uniform) and end (uniform) of FE/structural changes to be captured. These local results are significant as they demonstrate that the structure of CSTO (x = 0.2) still retains some C character at room temperature even though the longer-range structure, probed via XRD and Raman, appears T (Fig. S3, ESI†). This presence of C nature contributes to ferroelectricity suppression in this T phase as seen in literature.[57] Further increasing the concentration to x = 0.8 results in similar behavior to PTO, i.e., negligible response with temperature followed by a noticeable decrease in the standard deviation (between -100 to -80 °C), suggesting an overall increase in crystal uniformity throughout the NP.

Next, the CSNO samples were subjected to the same temperature-dependent measurements (Fig. 4d-f). There is a similar trend in the PL spectra for the CSNO as in the CSTO samples at all doping concentrations. However, for the concentration x = 0.2, there is an initial high R-value drop-off, which can also be seen in the BTO sample at ~50 °C, highlighting a possible similarity in their short-range structures. From this, it can be concluded that there is a difference in the long-range ordering, and respective phase transformations, in the CSNO crystals as a function of Ca doping. Additionally, despite the presence of oxygen vacancies from the low-pressure synthesis, this comparison with CSTO, BTO, and PTO NPs suggests that

these materials (CSNO) have the potential to exhibit FE phase transitions upon Ca doping, but further PFM measurements are needed. Overall, unlike PFM, *in-situ/ex-situ* PL measurements provide valuable information about the impact of synthesis conditions on the local and long-range structure which can be leveraged to quickly screen for FE-type phase transitions in next generation materials.

4. Conclusions

In summary, a novel approach to study local site symmetry transformations in ABO_3 perovskite NPs has been demonstrated. The low-loss response of $SrNbO_3$ makes it a promising candidate material for FE applications. Unfortunately, its centrosymmetric crystal structure suppresses FE distortions, motivating the use of defect chemistry to break the local A/B-site symmetry. This work highlights the crystallization and study of a potential FE material, i.e. CSNO, which cannot be synthesized using traditional wet-chemical methods. *In-situ/ex-situ* PL coupled with XRD and XAS analyses shows that this synthetic method limits available oxygen during the crystallization process lowering the A-site symmetry (R = 6.0 ± 0.1 to 4.4 ± 0) and facilitating FE/structural disorder. These values, when compared against the model system (CSTO, 2.7 ± 0.1 to 4.7 ± 0.1), non-FE (STO, R = 2.7 ± 0.1), and prototypical FEs (BTO, R = 4.8 ± 0.1 and PTO, R = 3.6 ± 0.1), further demonstrate that these defect-controlled CSNO NPs possess low-symmetry environments favorable for FE distortions. Ultimately, this ability to probe the local site symmetry of low-dimensional ABO_3 perovskites, will significantly impact the renewable energy industry by contributing to the design of Pb-free FE materials.

Conflicts of interest

There are no conflicts to declare.

Acknowledgements

T.O. acknowledges the fellowship support from the Louisiana College of Engineering and CHE-1709902 for supplies. K.R.B. acknowledge the Louisiana Board of Regents (LEQSF(2016–19)-RD-A-03) for financial support. The authors also acknowledge the support of the staff of the CAMD synchrotron light source.

Author Contributions

T.O. performed the synthesis of the Eu-doped CSNO, CSTO, BTO, and PTO nanoparticle samples, and completed the XRD, XAS, and PL analysis. K.R.B. performed the lifetime measurements, contributed to the PL analysis, and provided insight regarding the *in-situ*/*ex-situ* PL measurements. S.A.J.T. performed *in-situ*/*ex-situ* PL measurements. T.O. and O.K. performed the XAS measurements. A.T.M. and J.A.D. provided financial support and useful discussions. T.O. and J.A.D. conceived the project of using photoluminescence to detect defect-induced structural transformations in low-dimensional ABO_3 perovskites.

References

1. F. Cebulla, J. Haas, J. Eichman, W. Nowak and P. Mancarella, *J. Clean. Prod.*, 2018, **181**, 449-459.
2. M. D. Nguyen, E. P. Houwman and G. Rijnders, *J. Phys. Chem. C*, 2018, **122**, 15171-15179.
3. H. Pan, J. Ma, J. Ma, Q. Zhang, X. Liu, B. Guan, L. Gu, X. Zhang, Y.-J. Zhang and L. Li, *Nat. Commun.*, 2018, **9**, 1813.
4. A. Pramanick, W. Dmowski, T. Egami, A. S. Budisuharto, F. Weyland, N. Novak, A. D. Christianson, J. Borreguero, D. L. Abernathy and M. R. V. Jørgensen, *Phys. Rev. Lett.*, 2018, **120**, 207603.
5. N. A. Benedek and C. J. Fennie, *J. Phys. Chem. C*, 2013, **117**, 13339-13349.
6. C. W. Rischau, X. Lin, C. P. Grams, D. Finck, S. Harms, J. Engelmayer, T. Lorenz, Y. Gallais, B. Fauqué and J. Hemberger, *Nat. Phys.*, 2017, **13**, 643.
7. R. K. Vasudevan, N. Balke, P. Maksymovych, S. Jesse and S. V. Kalinin, *Appl. Phys. Rev.*, 2017, **4**, 021302.
8. F. Cordero, F. Trequattrini, F. Craciun, H. Langhammer, D. Quiroga and P. Silva Jr, *Phys. Rev. B*, 2019, **99**, 064106.
9. A. Sarantopoulos, W.-L. Ong, J. A. Malen and F. Rivadulla, *Appl. Phys. Lett.*, 2018, **113**, 182902.
10. K. R Bajgiran, P. Darapaneni, A. T. Melvin and J. A. Dorman, *J. Phys. Chem. C*, 2019, **123**, 13027-13035.
11. K. Bajgiran, J. Dorman and A. Melvin, *ACS Sens.*, 2020, **5**, 29.
12. K. O'Donnell, P. Edwards, M. Yamaga, K. Lorenz, M. Kappers and M. Boćkowski, *Appl. Phys. Lett.*, 2016, **108**, 022102.
13. B. Mitchell, D. Lee, A. Koizumi, J. Poplawsky, Y. Fujiwara and V. Dierolf, *Phys. Rev. B*, 2013, **88**, 121202.
14. B. Mitchell, J. Poplawsky, D. Lee, A. Koizumi, Y. Fujiwara and V. Dierolf, *J. Appl. Phys.*, 2014, **115**, 204501.
15. D. Lee, B. Mitchell, Y. Fujiwara and V. Dierolf, *Phys. Rev. Lett.*, 2014, **112**, 205501.
16. A. Stanulis, A. Katelnikovas, A. N. Salak, P. Seibutas, M. Ivanov, R. Grigalaitis, J. Banys, A. Kareiva, R. Ramanauskas and A. R. Barron, *Inorg. Chem.*, 2019, **58**, 11410-11419.
17. P. A. Tanner, *Chem. Soc. Rev.*, 2013, **42**, 5090-5101.
18. K. Bi, M. Bi, Y. Hao, W. Luo, Z. Cai, X. Wang and Y. Huang, *Nano Energy*, 2018, **51**, 513-523.
19. Y. Wang, P. Darapaneni, O. Kizilkaya and J. A. Dorman, *Inorg. Chem.*, 2020.
20. Y. S. Kim, D. Kim, T. Kim, T. Noh, J. Choi, B. Park and J.-G. Yoon, *Appl. Phys. Lett.*, 2007, **91**, 042908.
21. H. W. Jang, A. Kumar, S. Denev, M. D. Biegalski, P. Maksymovych, C. W. Bark, C. T. Nelson, C. M. Folkman, S. H. Baek, N. Balke, C. M. Brooks, D. A. Tenne, D. G. Schlom, L. Q. Chen, X. Q. Pan, S. V. Kalinin, V. Gopalan and C. B. Eom, *Phys. Rev. Lett.*, 2010, **104**, 4.
22. M. O. Ramirez, T. T. Lummen, I. Carrasco, E. Barnes, U. Aschauer, D. Stefanska, A. Sen Gupta, C. De Las Heras, H. Akamatsu and M. Holt, *APL Mater.*, 2019, **7**, 011103.
23. D. Wan, B. Yan, J. Chen, S. Wu, J. Hong, D. Song, X. Zhao, X. Chi, S. Zeng and Z. Huang, *Chem. Mater.*, 2019.
24. A. Paul and T. Birol, *Phys. Rev. Mater.*, 2019, **3**, 085001.

25. T. C. Asmara, D. Wan, Y. Zhao, M. A. Majidi, C. T. Nelson, M. C. Scott, Y. Cai, B. Yan, D. Schmidt and M. Yang, *Nat. Commun.*, 2017, **8**.
26. T. Zhang, W. Li, Y. Zhao, Y. Yu and W. Fei, *Adv. Funct. Mater.*, 2018, **28**, 1706211.
27. T. E. Beechem, M. D. Goldflam, M. B. Sinclair, D. W. Peters, A. E. McDonald, E. A. Paisley, A. R. Kitahara, D. E. Drury, D. B. Burckel and P. S. Finnegan, *Adv. Opt. Mater.*, 2018, **6**, 1800862.
28. D. Chen and J. Ye, *Chem. Mater.*, 2009, **21**, 2327-2333.
29. P. Darapaneni, N. S. Moura, D. Harry, D. A. Cullen, K. M. Dooley and J. A. Dorman, *J. Phys. Chem. C*, 2019, **123**, 12234-12241.
30. A. Testino, M. T. Buscaglia, V. Buscaglia, M. Viviani, C. Bottino and P. Nanni, *Chem. Mater.*, 2004, **16**, 1536-1543.
31. M. J. Campion, H. J. Brown-Shaklee, M. A. Rodriguez, J. J. Richardson, P. G. Clem and J. F. Ihlefeld, *J. Am. Ceram. Soc.*, 2013, **96**, 743-749.
32. T. Ofoegbuna, P. Darapaneni, S. Sahu, C. Plaisance and J. A. Dorman, *Nanoscale*, 2019, **11**, 14303-14311.
33. A. C. Larson and R. B. Von Dreele, General Structure Analysis System (GSAS), report LAUR 86-748, Los Alamos National Laboratory, NM, 1994.
34. B. Ravel and M. Newville, *J. Synchrotron Radiat.*, 2005, **12**, 537-541.
35. P. Darapaneni, O. Kizilkaya, Z. Wang and J. A. Dorman, *J. Phys. Chem. C*, 2018, **122**, 22699-22708.
36. J. A. Dorman, J. H. Choi, G. Kuzmanich, J. R. Bargar and J. P. Chang, *J. Appl. Phys.*, 2012, **111**, 083529.
37. P. Rez and A. Blackwell, *J. Phys. Chem. B*, 2011, **115**, 11193-11198.
38. F. De Groot, J. Fuggle, B. Thole and G. Sawatzky, *Phys. Rev. B*, 1990, **41**, 928.
39. K. Asokan, J. Jan, J. Chiou, W. Pong, M.-H. Tsai, Y. Chang, Y. Chen, H. Hsieh, H.-J. Lin and Y. Yang, *J. Solid State Chem.*, 2004, **177**, 2639-2643.
40. A. Borg, P. King, P. Pianetta, I. Lindau, D. Mitzi, A. Kapitulnik, A. Soldatov, S. Della Longa and A. Bianconi, *Phys. Rev. B*, 1992, **46**, 8487.
41. S. Jethva, S. Katba, M. Bhatnagar, M. Ranjan, D. Shukla and D. Kuberkar, *J. Appl. Phys.*, 2019, **125**, 082510.
42. M. Rini, Y. Zhu, S. Wall, R. Tobey, H. Ehrke, T. Garl, J. Freeland, Y. Tomioka, Y. Tokura and A. Cavalleri, *Phys. Rev. B*, 2009, **80**, 155113.
43. K. Kuepper, M. Falub, K. Prince, V. Galakhov, I. Troyanchuk, S. Chiuzbaian, M. Matteucci, D. Wett, R. Szargan and N. Ovechkina, *J. Phys. Chem. B*, 2005, **109**, 9354-9361.
44. F. De Groot, M. Grioni, J. C. Fuggle, J. Ghijsen, G. A. Sawatzky and H. Petersen, *Phys. Rev. B*, 1989, **40**, 5715.
45. T. Chen, L. Bao, Y. Zheng, X. Yang, L. Ruan, Y. Liu, G. Xu and G. Han, *CrystEngComm*, 2019, **21**, 4763-4770.
46. B. Im, H. Jun, K. H. Lee and J. S. Lee, *CrystEngComm*, 2011, **13**, 7212-7215.
47. H. W. Lee, S. Moon, C. H. Choi and D. K. Kim, *J. Am. Ceram. Soc.*, 2012, **95**, 2429-2434.
48. X.-H. Ma, H.-Y. Li, S.-H. Kweon, S.-Y. Jeong, J.-H. Lee and S. Nahm, *ACS Appl. Mater. Interfaces*, 2019, **11**, 5240-5246.
49. S. Qin, A. I. Becerro, F. Seifert, J. Gottsmann and J. Jiang, *J. Mater. Chem.*, 2000, **10**, 1609-1615.
50. F. A. Rabuffetti, H.-S. Kim, J. A. Enterkin, Y. Wang, C. H. Lanier, L. D. Marks, K. R. Poeppelmeier and P. C. Stair, *Chem. Mater.*, 2008, **20**, 5628-5635.
51. S. Qin, X. Wu, F. Seifert and A. I. Becerro, *J. Chem. Soc., Dalton Trans.*, 2002, 3751-3755.
52. J. Goethals, A. Bedidi, C. Fourdrin, M. Tarrida and S. Rossano, *Phys. Chem. Miner.*, 2019, **46**, 1003-1015.
53. C. Jiang, L. Fang, M. Shen, F. Zheng and X. Wu, *Appl. Phys. Lett.*, 2009, **94**, 071110.
54. Y. F. Wu, Y. T. Nien, Y. J. Wang and I. G. Chen, *J. Am. Ceram. Soc.*, 2012, **95**, 1360-1366.
55. E. Sawaguchi and M. L. Charters, *Phys. Rev.*, 1960, **117**, 465.
56. J. Kobayashi, Y. Uesu and Y. Sakemi, *Phys. Rev. B*, 1983, **28**, 3866.
57. T. Mitsui and W. B. Westphal, *Phys. Rev.*, 1961, **124**, 1354.
58. G. Geneste and J.-M. Kiat, *Phys. Rev. B*, 2008, **77**, 174101.
59. D. Yang, D. Chen, H. He, Q. Pan, Q. Xiao, J. Qiu and G. Dong, *Sci. Rep.*, 2016, **6**, 29871.
60. M. Vaithiyanathan, K. R. Bajgiran, P. Darapaneni, N. Safa, J. A. Dorman and A. T. Melvin, *Anal. Bioanal. Chem.*, 2019, **411**, 157-170.

Table of Content Graphic

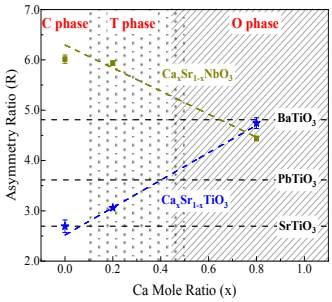

Photoluminescence detection of symmetry transformations in low-dimensional ABO_3 Perovskites.